Applied Catalysis B: Environmental 313 (2022) 121458

Contents lists available at ScienceDirect

Applied Catalysis B: Environmental

journal homepage: www.elsevier.com/locate/apcatb

MoS_2 nanosheet integrated electrodes with engineered 1T-2H phases and defects for efficient hydrogen production in practical PEM electrolysis

Zhiqiang Xie [a,1], Shule Yu [a,1], Xiaohan Ma [b,c,1], Kui Li [a], Lei Ding [a], Weitian Wang [a], David A. Cullen [b,*], Harry M. Meyer III [d], Haoran Yu [b], Jianhua Tong [c], Zili Wu [b,d], Feng-Yuan Zhang [a,*]

[a] Nanodynamics and High-Efficiency Lab for Propulsion and Power (NanoHELP), Department of Mechanical, Aerospace & Biomedical Engineering, UT Space Institute, University of Tennessee, Knoxville, TN 37388, USA
[b] Center for Nanophase Materials Sciences, Oak Ridge National Laboratory, Oak Ridge, TN 37831, USA
[c] Department of Materials Science and Engineering, Clemson University, Clemson, SC 29634, USA
[d] Chemical Science Division, Oak Ridge National Laboratory, Oak Ridge, TN 37831, USA

ARTICLE INFO

Keywords:
Ionomer-free integrated electrodes
1T-2H heterophase
Defect-rich MoS_2 nanosheets
Hydrogen evolution reaction
PEM water electrolysis

ABSTRACT

Low electrical conductivity and poor accessibility of MoS_2 reaction sites raise great challenges in maximizing the triple-phase-boundary (TPB) sites of MoS_2-based electrodes and minimizing ohmic losses for efficient hydrogen evolution reaction (HER) in practical proton exchange membrane (PEM) water electrolysis. Herein, we report a scalable hydrothermal approach to fabricate ionomer-free integrated electrodes with engineered 1 T-2 H heterophase and defect-rich MoS_2 nanosheets (MoS_2NSs) *in-situ* grown onto the carbon fiber paper (CFP). With an ultralow loading of 0.14 mg/cm^2, a small voltage of 2.25 V was obtained at 2000 mA/cm^2 in a practical cell with Nafion115 membrane, which outperforms all previously reported high-loading non-precious catalyst-based electrodes. Impressively, it shows 44 times higher mass activity than a high-loading and ionomer-mixed MoS_2 assemblies electrode. This work builds a bridge from catalyst optimization to electrode fabrication and provides a promising direction for improving intrinsic catalytic activity, electrode conductivity and stability for practical PEM water electrolysis.

1. Introduction

A proton exchange membrane electrolyzer cell (PEMEC) stands out as a promising technique to efficiently generate high-purity hydrogen from various renewable energy resources [1–4]. At present, the benchmarking catalysts for electrocatalytic water electrolysis are platinum and iridium-based nanostructured materials [5,6]. Nevertheless, the practical application of PEMECs remains challenging due to the high platinum group metal (PGM) loading (1–3 mg/cm^2), scarcity of supply and costly electrode fabrication [7–10]. Therefore, it is highly urgent yet challenging to develop PGM-free or ultralow PGM-loaded electrocatalysts with competitive catalytic activity, durability and low cost. Currently, layered transition metal dichalcogenides (TMDCs) have demonstrated a potential substitute for costly Pt as HER electrocatalysts in water splitting, thanks to its high intrinsic activity of metallic edges ($\Delta G_H = 0.08$ eV) and high abundance [11–16]. Unfortunately, its high hydrogen adsorption free energy within basal-plane and low electronic conductivity lead to overall low catalytic activities and thus largely prevent their utilization in practice [17–21].

Nanostructure and defect engineering are two commonly used strategies for further maximizing the number of active reaction sites for HER by creating numerous exposed edges, pinholes and atomic sulfur vacancies within basal planes of MoS_2 [22–30]. More recently, phase engineering of MoS_2 from semiconducting 2 H phase into more catalytically active 1 T phase by doping, plasma treatment and flash Joule heating can greatly enhance the intrinsic catalytic activities due to the excellent conductivity of metallic 1 T phase [31–35]. However, most methods reported up to date are of very limited application in practical water electrolyzers, mainly owing to their manipulation/synthesis complexity, poor scalability and high ohmic losses in the real cell. Furthermore, due to low intrinsic catalytic activity and conductivity, very high MoS_2 based catalyst loadings (3–6 mg/cm^2) are usually required in water electrolyzers to achieve acceptable cell performances at high current densities, leading to very limited cost reduction

* Corresponding authors.
E-mail addresses: cullenda@ornl.gov (D.A. Cullen), fzhang@utk.edu (F.-Y. Zhang).
[1] These authors contributed equally to this work.

https://doi.org/10.1016/j.apcatb.2022.121458
Received 3 February 2022; Received in revised form 9 April 2022; Accepted 25 April 2022
Available online 27 April 2022

compared to PGM-based catalysts [36–40].

To address the above challenges, we fabricate the integrated HER electrode comprising *in-situ* grown 1 T-2 H MoS_2 ultrathin nanosheets onto highly conductive carbon paper with rich engineered defects *via* precisely tuning the hydrothermal synthesis parameters. The unique advantages are as follows: (a) Ideal 1 T-2 H phase integration can combine the excellent structural stability of 2 H phase and the high conductivity of metastable 1 T phase to activate the inert MoS_2 basal-planes; (b) Highly defective ultrathin nanosheets with rich exposed edges and additional basal-plane defects (pinholes, atomic sulfur vacancies) can further maximize the active sites; (c) *In-situ* growth method enables the intimate contact and strong adhesion of MoS_2 nanosheets and 3D porous conductive carbon support, resulting in significant reduction of ohmic losses and mass transport losses and remarkable stability enhancement in the practical electrolyzer cell. Benefitting from the above synergistic effects, the defect-rich 1 T-2 H MoS_2/CFP integrated electrode with an extremely low catalyst loading of 0.14 mg/cm^2 not only shows significantly improved HER performances in liquid acidic electrolyte, but also demonstrates outstanding cell performances in practical PEMECs. Under 1 and 2 A/cm^2, the required cell voltages are only 1.96 and 2.25 V, respectively. Such remarkable cell performances are superior to almost all non-precious HER catalysts with extremely high loadings of 3–6 mg/cm^2 under the similar cell operation conditions in the literatures. We believe this work builds up a bridge to connect catalyst optimization to electrode fabrication, which provides new insights into how to concurrently enhance the intrinsic catalytic activity, whole electrode conductivity and electrochemical stability for low-cost hydrogen production under high current densities in practical water electrolyzers.

2. Experimental section

2.1. Fabrication of defect-rich 1T-2H MoS_2 nanosheet integrated electrodes

The 0.6 g sodium molybdate dihydrate ($Na_2MoO_4{\cdot}2H_2O$) and 1.2 g thioacetamide (C_2H_5NS) were dissolved in deionized water (20 mL) under continuous stirring at room temperature for 30 min. Then, the above 20 mL solution was added into a Teflon-lined autoclave (50 mL). The carbon fiber paper was vertically immersed into the reactor. Afterwards, the autoclave was well sealed and kept heating to 220 °C for 24 h in a box oven. After cool-down of the autoclave to room temperature for another 24 h, the sample was obtained and washed with water and alcohol for at least three times. Finally, the defect-rich 1 T-2 H MoS_2NS/CFP was obtained after drying at 60°Covernight. For comparison, MoS_2 assemblies/CFP electrodes were fabricated by a conventional spray coating method. The spray coated catalyst layer was composed of 80 wt% MoS_2 assembly powders and 20 wt% Nafion ionomer binders. The loading of MoS_2 assemblies was controlled to be 3.0 mg/cm^2 on the CFP support. The geometric area of MoS_2 assemblies/CFP electrode was 5 cm^2.

2.2. Characterizations

The SEM morphology and elemental mapping images were obtained from Zeiss Merlin scanning electron microscope coupled with energy-dispersive X-ray spectroscopy (EDX) detector from Oxford Instruments. The detailed structural information was characterized by aberration-corrected scanning transmission electron microscopy (STEM) on a JEOL JEM-ARM200F "NEOARM" operated at an acceleration voltage of 80 kV. The surface chemistry and phase composition were identified by X-ray photoelectron spectroscopy (XPS) analysis on a Thermo Scientific K-Alpha spectrometer. Raman spectroscopy was conducted on a multiwavelength Raman system at room and elevated temperatures. Raman scattering was measured by a triple Raman spectrometer (Princeton Instruments Acton Trivista 555). The 532 nm laser was applied as the excitation beam with a 30 s exposure time and 10 times accumulations. The sample stage is movable with a zigzag style in a dimension of 4 mm * 4 mm to check the homogeneity of measured sample.

2.3. Electrochemical measurements

The HER performances of defect-rich 1 T-2 H MoS_2/CFP and spray coated MoS_2 assemblies/CFP were compared *via ex-situ* electrochemical measurements in 0.5 M H_2SO_4 liquid electrolyte. Before electrochemical measurements, the electrolyte was de-aerated by continuously bubbling of high-purity Ar gas for at least 1 h. The as-prepared defect-rich 1 T-2 H MoS_2/CFP or spray coated MoS_2 assemblies/CFP was employed as the working electrode, a graphite rod as the counter electrode and the Ag/AgCl reference electrode were used in the three-electrode system. The linear sweep voltammetry (LSV) data were collected by a Potentiostat (Bio-Logic) at a scan rate of 5 mV s^{-1}. Chronopotentiometry (CP) test of the working electrode was carried out under − 10 mA/cm^2 for 38 h. The electrochemical impedance spectroscopy (EIS) measurements were obtained between 100 KHz and 50 mHz.

2.4. The PEMEC assembly and testing

For the assembly of the PEMEC, the defect-rich 1 T-2 H MoS_2NS/CFP electrode or spray coated MoS_2 assemblies/CFP with the geometric area of 5 cm^2 was sandwiched between PEM surface and AXF-5Q graphite bipolar plate at cathode. The catalyst-coated membrane (CCM) with 3 mg/cm^2 $IrRuO_x$ catalyst (FuelCellEtc) coated on a Nafion 115 membrane (~127 μm in thickness) and a titanium-made liquid/gas diffusion layer (LGDL) were adopted at anode for all cell tests. Two stainless steel made endplates were used to compress the PEMEC (4.52 N•m of torque). The PEMEC performance comparison between defect-rich 1 T-2 H MoS_2NS/CFP electrode and spray coated MoS_2 assemblies/CFP were carried out at 80 °C and atmosphere pressure with a water flow rate of 20 mL min^{-1} at anode. The active area of the PEMEC was controlled to be 5 cm^2. As the baseline, commercial CCMs with IrRuOx (3.0 mg/cm^2) at the anode, Pt/C (0.2 mg_{Pt} cm^{-2}) at the cathode, and Nafion 115 with a thickness of 127 μm as the PEM were tested in the PEMEC. The polarization curves were measured on a Potentiostat (VSP/VMP3B-100, Bio-Logic). The EIS plots were recorded under 0.2 A cm^{-2} between 100 KHz and 50 mHz.

3. Results and discussion

3.1. Structure and morphology of defect-rich 1T-2H MoS_2

As depicted in Fig. 1**a**, a conventional PGM-free electrode for the HER in a PEMEC is commonly fabricated by the spray coating of ionomer-mixed catalyst ink onto the 3D porous media such as CFP substrate. In this electrode, large MoS_2 assemblies and a certain quantity of Nafion binders are mixed together to form a non-uniform catalyst layer on the CFP substrate. Thus, the required TPB sites for the HER are insufficient due to the difficult accessibility of active MoS_2 edges. Furthermore, the whole electrode usually suffers from poor electrical conductivity, leading to large ohmic losses and low efficiencies of hydrogen production in a PEMEC. To this end, as illustrated in Fig. 1**b**, we design and synthesize novel MoS_2 ultrathin nanosheets *in-situ* grown on CFP with desirable phase composition, defects and morphology *via* a one-step hydrothermal method, forming the defect-rich 1 T-2 H MoS_2NS/CFP integrated electrode for both liquid and solid electrolyte-based water electrolyzers.

During the electrode fabrication, sodium molybdate dihydrate ($Na_2MoO_4{\cdot}2H_2O$) as the Mo source, thioacetamide (C_2H_5NS) as the S source and water as the only solvent were employed for synthesis of mixed 1 T-2 H MoS_2 nanosheets onto the CFP substrate, without requirement of any additive, pH adjuster and stabilizer. Based on the literatures, Mo (IV) species play a dominant role in the formation of 1 T-

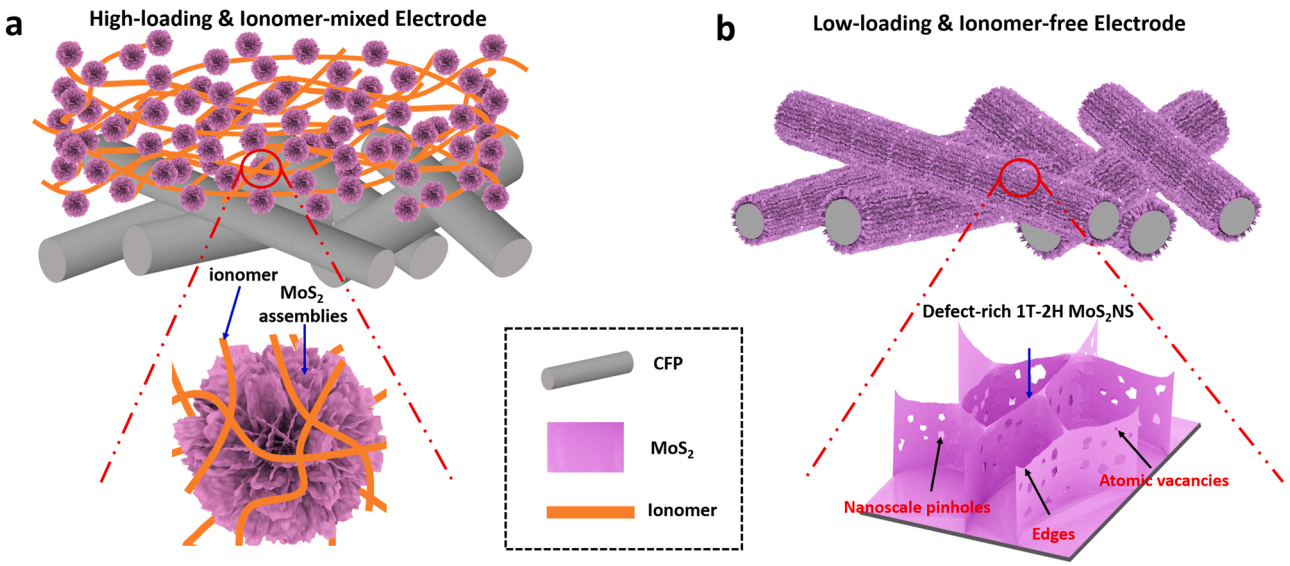

Fig. 1. Schematic illustration of PGM-free electrode designs for the HER in a PEMEC. (a) A conventional electrode with spray coated high-loading MoS_2 powders mixed with ionomer. (b) Ionomer-free electrode with *in-situ* grown ultralow-loading and defect-rich 1T-2H MoS_2 nanosheets.

phase MoS_2 under hydrothermal or solvothermal conditions [41,42]. The proposed formation mechanism of 1 T-2 H MoS_2 nanosheets is as follows. Initially, Mo (VI) species are reduced to Mo (IV), which usually appears in an octahedral coordination in $[MoO_6]$. Subsequently, the sulfurization proceeds by replacement of O^{2-} ligands in the $[MoO_6]$, resulting the 1 T-phase MoS_2 with the retained octahedral coordination structure. With the prolonged reaction time, the consumption of the CS $(NH_2)_2$ leads to the reduced Mo (IV) species, which allows the formation of the 2 H-phase MoS_2. Finally, the integration of 1 T and 2 H phases is *in-situ* grown on the CFP. The defects within 1 T-2 H MoS_2 nanosheets are formed during the synthesis because of the excess thiourea, which can restrict the oriented crystal growth *via* adsorption on the surface of MoS_2 primary nanocrystals to some extent.

Within such integrated electrode, the catalytic activity and durability of MoS_2 catalysts are expected to be boosted because of the following unique merits: First, the improvement of charge transfer from substrate to catalytic sites and electrode durability could be achieved by eliminating the contact resistance and increasing the adhesion between catalysts and underlying substrate *via in-situ* growth strategy. Second, MoS_2 catalysts with integrated 1 T and 2 H phases could further combine the high electrical conductivity of 1 T phase and excellent structural stability of 2 H phase, thereby leading to enhanced conductivity and activation of MoS_2 catalyst layers. Third, ultrathin nanosheets are enriched with various defects such as exposed edge sites, basal-plane pinholes and atomic vacancies, which can offer a large number of active sites due to their favorable free hydrogen adsorption energy [43–45].

The CFP substrate is composed of individual carbon fibers with relatively smooth surfaces, as shown in Fig. 2**a**. The high-resolution SEM images in Fig. 2**b** and **c** indicate the successful growth of numerous vertically aligned nanosheets on the CFP substrate with a large quantity

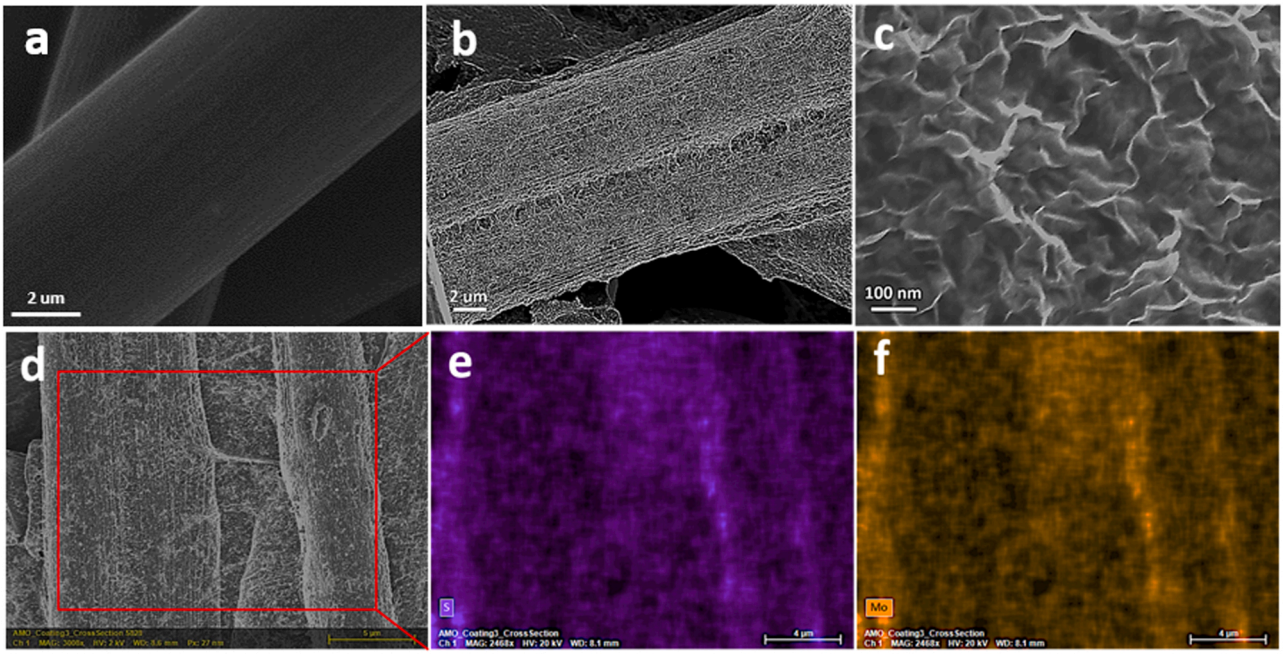

Fig. 2. (a) SEM image of CFP. (b, c, d) typical SEM images of defect-rich 1T-2H MoS_2NS/CFP, and SEM-EDX mapping images of (e) S and (f) Mo, respectively.

of exposed edge sites. The SEM-EDX mapping images in Fig. 2**d-e** verify the homogenous elemental distribution of S and Mo in the integrated electrode. The photograph of the defect-rich 1 T-2 H MoS_2NS/CFP sample is shown Fig. S1. Due to its low cost and easy experimental setup, the employed hydrothermal synthesis method in this work can be applied to fabricate customized sizes of samples with various substrates. By comparison, the SEM images in Fig. S2 show that conventional spray coated MoS_2 assemblies/CFP are composed of large assemblies on the CFP with Nafion ionomer binders, and the ionomer mixed catalyst layer is not uniform across the entire electrode. The non-uniformity and large assemblies of the MoS_2 catalyst layer on the CFP would give rise to a poor interfacial contact between catalyst layer and solid PEM electrolyte, thereby resulting in insufficient TPB sites for reactions and large ohmic losses in a PEMEC.

To better visualize the nanostructure of MoS_2 nanosheets, the HAADF-STEM characterizations were carried out. As seen from Fig. 3**a-c**, highly distorted edges such as folds, sharp vertices and propagating ridges are all identified within different MoS_2 nanosheets. The lateral size of nanosheets is estimated to be 50 ~ 100 nm. The calculated thickness of the whole nanosheets is about 3.9 ~ 5.2 nm, corresponding to 6 ~ 8 layers of MoS_2. To further scrutinize the structure of MoS_2 basal planes at nanoscale, the areas both near the edges and on the basal plane are highlighted in Fig. 3**d-f**. Interestingly, it is found that nanoscale pinholes (1–2 nm) and atomic vacancies co-exist on the basal plane, as marked by yellow and red dash lines. Furthermore, as seen from Fig. 3**e** and **f**, the edges of nanosheets with a few clear steps in the flat area indicate that edges of MoS_2 nanosheets are mainly composed of 1–3 layers. It is noted that the presence of bilayer MoS_2 is also verified, as marked by a purple dash line in Fig. 3**f**.

3.2. Phase and chemical states of defect-rich 1T-2H MoS_2

The XPS was performed to analyze the surface chemistry and phase composition of defect-rich 1 T-2 H MoS_2/CFP integrated electrode. The full survey in Fig. S3 shows the overall surface composition of Mo, S, O, C and a small amount of N. As seen from the high-resolution XPS spectra of Mo 3d+S 2 s in Fig. 4**a**, the Mo 3d, which overlaps with S 2 s, shows several features. One Mo 3d doublet is assigned to the "1 T", and a second Mo doublet is assigned to "2 H". These results are well consistent with the literatures [29,46–48]. Along with them, two Mo satellites belonging to the "1 T" and "2 H" configurations and two S 2 s peaks are also observed. Based on the calculation from the peak fit for high-resolution spectra of Mo 3d, the 1 T/2 H phase ratio is determined to be 1.56, indicating that 1 T phase is predominant in MoS_2 nanosheets. In Fig. 4**b**, the high-resolution XPS spectra of S 2p show two doublets. One is assigned to S-Mo and the other is assigned to S-C bonding. The presence of S-C bonding verifies the *in-situ* growth of MoS_2 onto CFP instead of physical deposition or coating. This strong chemical bonding between MoS_2 and CFP support ensures good electrode durability during long-term operation in practical water electrolyzers. Additional evidence of C-S bonding in Fig. 4**c** also indicates the existence of chemical bonding between catalyst and CFP. The high-resolution of C 1 s shows the presence of both C-C bonding and C-S bonding. Interestingly, the high-resolution XPS spectra of Mo $3p_{3/2}$ + N 1 s in Fig. 4**d** displays the nitride species at 399.6 eV and protonated N at 401.6 eV. Raman spectroscopy was utilized to further confirm the phase composition of MoS_2 in defect-rich 1 T-2 H MoS_2/CFP integrated electrode. As seen from Fig. S4. the distinct peak at 150 cm^{-1} is likely attributed to a plasma line from the laser and the J_1 mode of 1 T phase might be buried under. The distinct phonon modes at 218 cm^{-1} (J_2) and 327 cm^{-1} (J_3) can be assigned to the 1 T super lattice structure. The broadening of 407 cm^{-1} ($A_{1\,g}$) and 376 cm^{-1} ($E^1_{2\,g}$) modes are mainly attributed to the 2 H phase of MoS_2. Therefore, ultrathin MoS_2 nanosheets in the integrated electrode are composed of both 1 T and 2 H phases.

The above SEM, HAADF-STEM, XPS and Raman characterizations collectively reveal that 1 T-2 H MoS_2 nanosheets with rich defects such as exposed highly distorted edges, basal-plane pinholes and atomic vacancies are successfully *in-situ* grown on CFP substrate, with strong

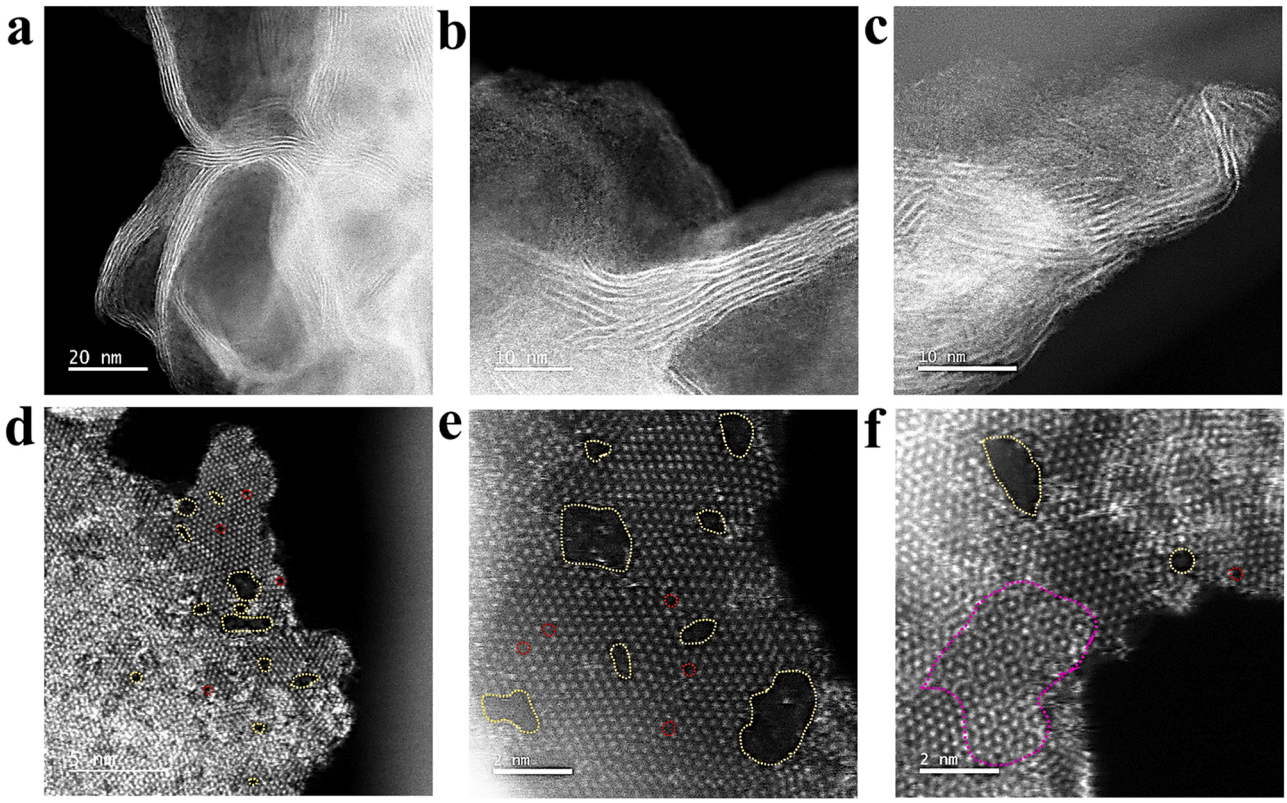

Fig. 3. HAADF-STEM images of defect-rich 1T-2H MoS_2NS/CFP, confirming the co-existence of edges, pinholes & atomic vacancies.

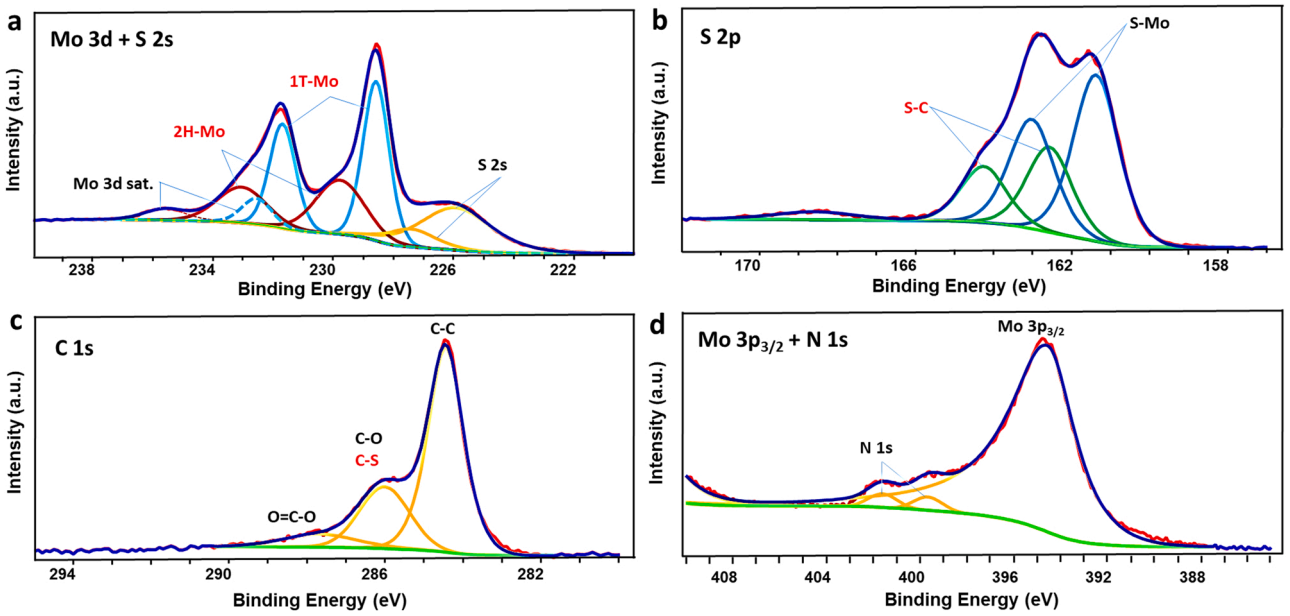

Fig. 4. High-resolution XPS spectra of defect-rich 1T-2H MoS_2NS/CFP. (a) Mo 3d+S 2s, (b) S 2p, (c) C 1s and (d) Mo 3p+N 1s, respectively.

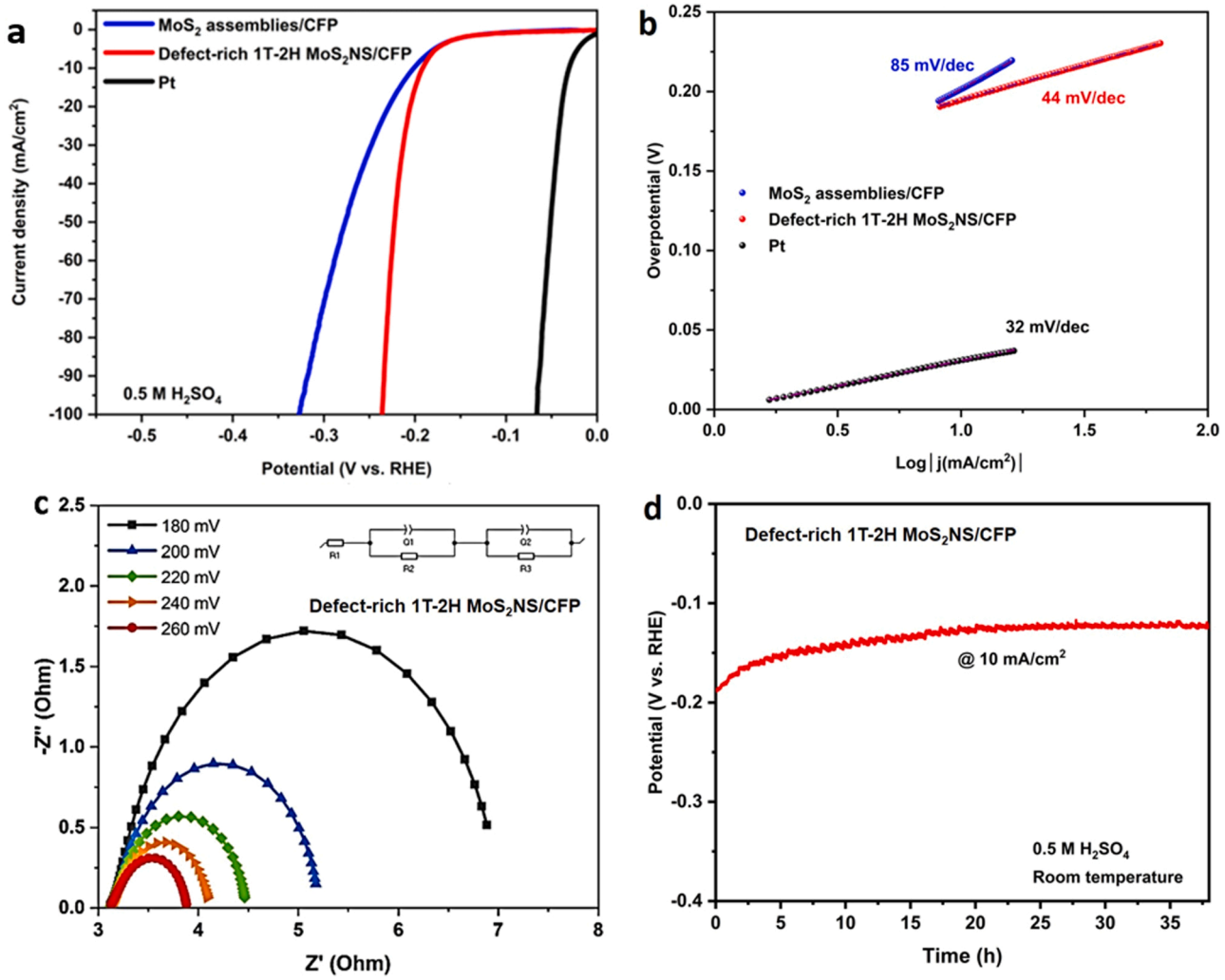

Fig. 5. (a) Polarization curves of defect-rich 1T-2H MoS_2NS/CFP and MoS_2 assemblies/CFP. (b) Corresponding Tafel plots. (c) Nyquist plots of defect-rich 1T-2H MoS_2NS/CFP at various overpotentials. (d) Electrode stability test of defect-rich 1T-2H MoS_2NS/CFP at 10 mA/cm^2 for over 38 h.

chemical coupling between catalyst layer and conductive substrate. We hypothesize that the synergistic effects from rich defects, integration of 1 T-2 H phase and ultrathin nanosheets chemically bonded onto CFP would activate conventional "inert" 2 H-MoS_2 basal planes with additional more catalytically active sites and meanwhile enhance both internal and interfacial electronic conductivity between MoS_2 catalyst layer and the substrate [43]. Therefore, both catalytic activity and durability of the integrated electrode are boosted for HER application in practical acidic water electrolyzers.

3.3. Catalytic performances in liquid electrolyte

To validate our hypothesis, *ex-situ* electrochemical characterizations of defect-rich 1 T-2 H MoS_2/CFP integrated electrode and spray coated MoS_2 assemblies/CFP were conducted in 0.5 M H_2SO_4 at room temperature. The MoS_2 catalyst loading in the integrated electrode is 0.14 mg/cm^2. As shown in Fig. 5**a** and **b**, the integrated electrode exhibits an extremely low overpotential of 192 mV and small Tafel slope of 44 mV/dec, outperforming MoS_2 assemblies/CFP and most previous results of MoS_2-based catalysts in the literatures. As seen from the Nyquist plots in Fig. 5**c**, the EIS analysis at various overpotentials displays similar impedance properties at each overpotential, suggesting that similar electrochemical processes occur at all overpotentials tested between 180 and 260 mV. By calculation, the defect-rich 1 T-2 H MoS_2/CFP shows very low charge transfer resistances of 3.679, 1.897, 1.145, 0.657 and 0.263 Ω at overpotentials of 180, 200, 220, 240 and 260 mV, respectively, indicating the ultrafast Faradaic process and a superior kinetics for HER. The measured small transfer resistances can be attributed to the synergetic effects of the integrated electrode, in which the intimate contact between MoS_2 and CFP ensures fast electron transport from CFP substrate to both MoS_2 edge sites and activated basal planes with more defects as active sites for HER. To study the electrode durability during long-term operation, the 38-hr electrochemical stability test at 10 mA/cm^2 was performed. As seen from Fig. 5**d**, gradual activation may proceed in the first 20 h and then the overpotential keeps stable for the rest of test. No obvious catalyst or electrode degradation is observed in liquid acidic electrolyte, indicating high electrode durability in long-term operation. There are two possible reasons for this gradual activation phenomenon. Firstly, we hypothesize that more liquid electrolyte may gradually penetrate into the whole catalyst layer and then increase more active sites for the HER in the first 20 h-testing. Afterwards, the liquid electrolyte may saturate the whole catalyst layer and stabilize the HER performance in the rest of 18 h-testing. Secondly, a possible surface reconstruction (*e.g.*, extra edge distortions and defects) may occur in MoS_2 nanosheets, probably creating more active sites for the HER and resulting in gradual activation of catalysts in the first 20 h-testing. However, such gradual activation phenomenon is still not fully understood. In the future, *in-situ* characterizations (*e.g.*, *in-situ* TEM and *in-situ* Raman) would be further investigated to better understand the gradual activation mechanism.

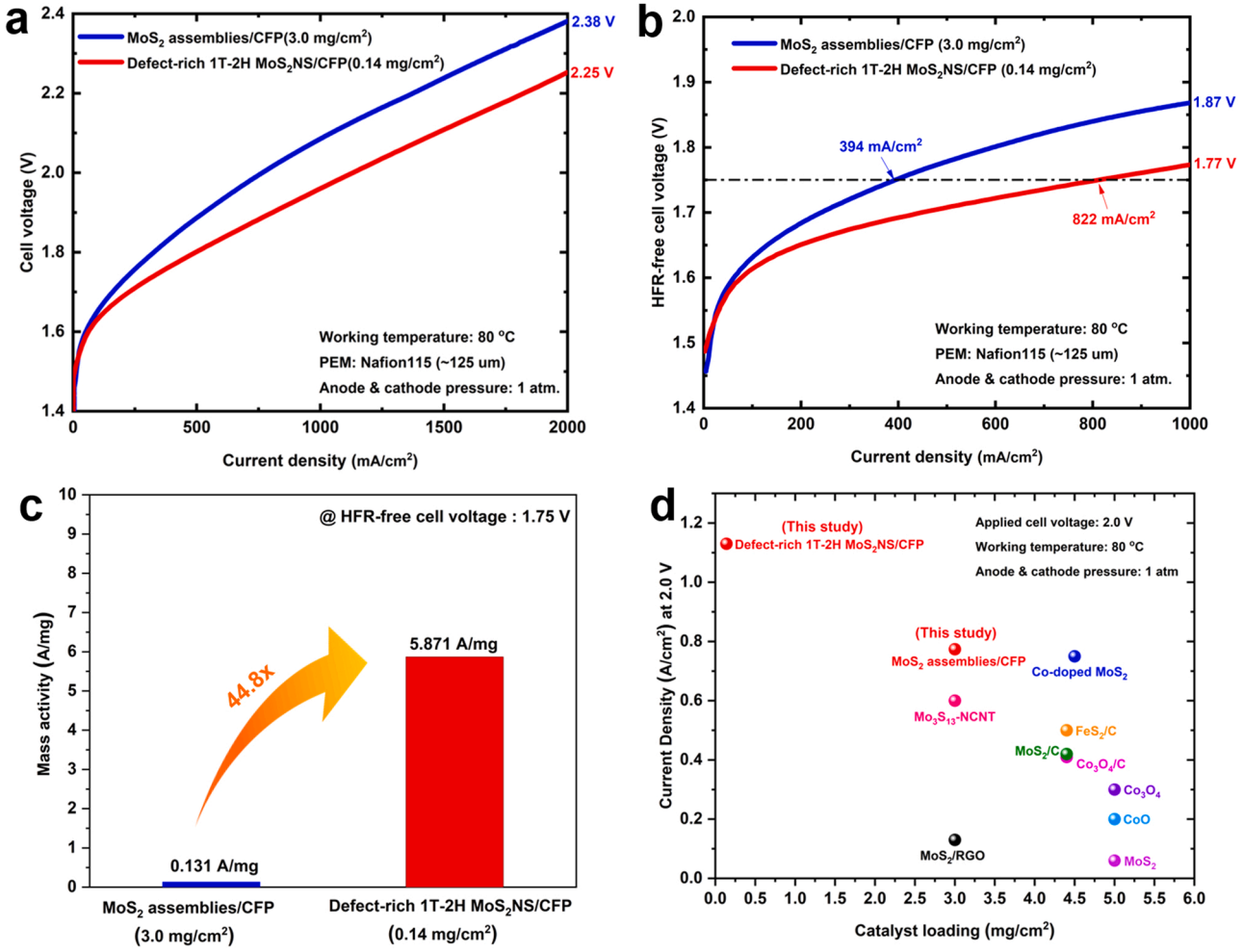

Fig. 6. (a) Polarization curves of defect-rich 1T-2H MoS_2NS/CFP and MoS_2 assemblies/CFP in a PEMEC at 80 °C. (b) HFR-free polarization curves. (c) Mass activity comparison at the HFR-free cell voltage of 1.75 V. (d) Comparison of achievable current densities under the same applied cell voltage of 2.0 V and working temperature of 80 °C between this study and previously reported non-precious cathode catalysts with different loadings in a PEMEC.

3.4. Full cell characterization in PEMECs

Fig. 6**a** shows the *in-situ* cell performance comparison of defect-rich 1 T-2 H MoS_2NS/CFP and MoS_2 assemblies/CFP in a PEMEC. By comparison, at 2000 mA/cm^2, defect-rich 1 T-2 H MoS_2NS/CFP with an ultralow loading of 0.14 mg/cm^2 demonstrates a much lower cell voltage of 2.25 V than that of MoS_2 assemblies/CFP (2.38 V). As seen from the HFR curves in Fig. S5, the average of HFR value of defect-rich 1 T-2 H MoS_2NS/CFP is about 187 mOhm*cm^2, which is smaller than that of MoS_2 assemblies/CFP (217 mOhm*cm^2), indicating the ohmic losses can be greatly reduced with defect-rich 1 T-2 H MoS_2NS/CFP electrode in a PEMEC. The HFR-free polarization curves in Fig. 6**b** further identify that the activation losses of defect-rich 1 T-2 H MoS_2NS/CFP electrode is significantly lower than MoS_2 assemblies/CFP, as evidenced by the cell voltage decrease of 100 mV at 1000 mA/cm^2. These results validate that defect-rich 1 T-2 H MoS_2NS/CFP possesses greatly maximized TPB sites and improved electrical conductivity compared to conventional spray coated electrodes.

By calculation of mass activities at HFR-free cell voltage of 1.75 V, it is found that the mass activity of defect-rich 1 T-2 H MoS_2NS/CFP is as high as 5.871 A/mg, which is over 44.8 times higher than that of a conventional spray coated electrode. Fig. 6**d** shows the comparison of achievable current densities under the same applied cell voltage of 2.0 V and working temperature of 80 °C between this study and previously reported PGM-free cathode catalysts with different catalyst loadings in PEMECs. It is clearly seen that our defect-rich 1 T-2 H MoS_2/CFP electrode can afford a significantly higher current density of 1.13 A/cm^2 at the applied cell voltage of 2.0 V than all previous studies in the literatures [36–40]. More importantly, our study shows that about 20–40 times lower loadings of nonprecious catalysts compared to previous publications can be achieved by using defect-rich 1 T-2 H MoS_2NS/CFP integrated electrode.

For performance comparison with commercial cathode catalysts, we also tested the commercial Pt/C catalyst with a similar loading of 0.2 mg/cm^2 under the identical conditions. By comparison of polarization curves in Fig. S6a, a commercial Pt/C catalyst-based cathode shows a lower cell voltage of ~ 2.18 V than that of a defect-rich 1 T-2 H MoS_2NS/CFP cathode (2.25 V). The hydrogen production rates for both defect-rich 1 T-2 H MoS_2NS/CFP and Pt/C catalysts were calculated and compared in Fig. S6b. At the applied cell voltage of 1.8 V, H_2 production of 0.13 g/h per mg cathode catalyst can be achieved for defect-rich 1 T-2 H MoS_2NS/CFP, which is lower than that of Pt/C catalysts (0.18 g/h per mg cathode catalyst). However, at the higher applied cell voltage of 2.0 V, defect-rich 1 T-2 H MoS_2NS/CFP displays a H_2 production rate of 0.30 g/h, which is comparable to Pt/C catalysts (0.28 g/h per mg cathode catalyst). Considering the earth-abundance and much lower price of MoS_2 materials than expensive PGM-based catalysts, the developed defect-rich 1 T-2 H MoS_2NS/CFP cathode in this work would hold great potential for large-scale water electrolyzer applications.

Fig. 7 shows the *in-situ* cell performance characterizations of defect-rich 1 T-2 H MoS_2/CFP as cathode in PEMECs tested under three typical working temperatures of 60, 80 and 90 °C. As a result, with an ultralow MoS_2 loading of 0.14 mg/cm^2, the obtained integrated electrode can afford high current densities of 1 A/cm^2 under 60, 80, and 90 °C by applying low cell voltages of 2.04, 1.96 and 1.91 V, respectively. Even at a higher current density of 2 A/cm^2, the applied cell voltages are only about 2.39, 2.25 and 2.19 V, respectively. These results demonstrate that defect-rich 1 T-2 H MoS_2NS/CFP can be directly applied as an efficient integrated cathode in PEMECs under the temperature range of 60–90 °C.

3.5. Post-analysis of defect-rich 1T-2H MoS_2 after electrolyzer test

Firstly, to unveil the morphological and structural changes of catalysts, the top-view and cross-sectional SEM and EDX as well as STEM characterizations of defect-rich 1 T-2 H MoS_2NS/CFP after the electrolyzer cell test were carried out. As seen from the top-view SEM images in Fig. S7a-**c,** although MoS_2 nanosheets aggregate in some areas of the CFP substrate, the vertically aligned nanosheets are still maintained and fully cover the entire surface of the substrate. The SEM-EDX mapping images in Fig. S7d-**f** display a relatively uniform distribution of S and Mo elements on the CFP substrate, suggesting no significant detachment of the catalyst layer from the substrate. The cross-sectional SEM and EDX mapping images in Fig. S8 further verify the good coverage of MoS_2 nanosheets on the CFP substrate surface, demonstrating good mechanical stability of as-synthesized defect-rich 1 T-2 H MoS_2NS/CFP in a practical PEMEC. Moreover, the HAADF-STEM images in Fig. S9 confirm that MoS_2 nanosheet structures and defects of distorted edges, nanoscale pinholes and atomic vacancies are still remained almost the same as the fresh sample before the electrolyzer cell test.

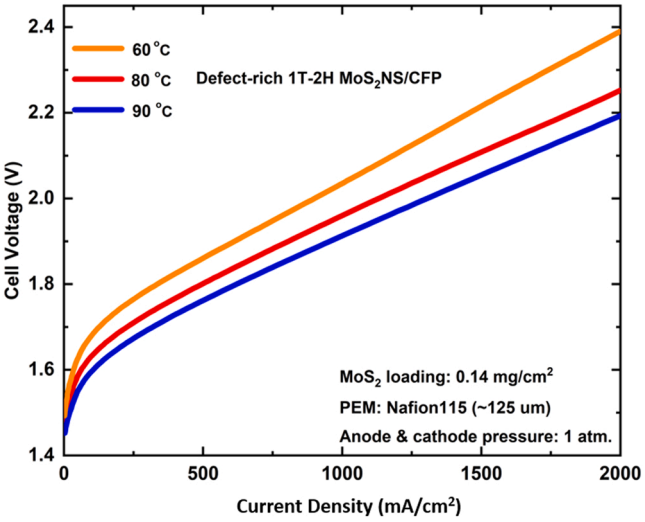

Fig. 7. *In-situ* cell performances of defect-rich 1T-2H MoS_2NS/CFP in a PEMEC under working temperatures of 60, 80 and 90 °C.

Secondly, the phase composition change of catalysts was also analyzed by the Raman spectroscopy and XPS techniques. Fig. S4 exhibits similar Raman spectra of defect-rich 1 T-2 H MoS_2NS/CFP electrode before and after the electrolyzer cell test, which indicates the 1 T and 2 H MoS_2 phases are retained after the electrolyzer cell test. The analysis of high-resolution XPS spectra of Mo 3d+S 2 s in Fig. S10a further reveal the slight decrease of 1 T/2 H phase ratio from 1.56 for the fresh sample to 1.33 for the tested sample. The partial 1 T phase conversion into the 2 H phase is probably attributed to the metastability of 1 T phase at 80 °C in a practical PEMEC [49–51]. The high-resolution XPS spectra of S 2p in Fig. S10b show the same two doublets with the fresh sample in Fig. 4**b**, which are assigned to S-Mo and S-C bonding. But it is found that the oxidized S content is increased from about 1.0 at% for the fresh sample to about 4.0 at% for the tested sample.

4. Conclusions

In summary, we report a scalable approach to create rich defects and 1 T-2 H hetero-phase into MoS_2 nanosheets, which were *in-situ* vertically grown onto the conductive CFP for the first time. The Raman and XPS characterizations verified the co-existence of 1 T and 2 H phases in the MoS_2 nanosheets. The 1 T phase is dominant and more conductive than 2 H phase in nature. The HAADF-STEM images further elucidate the rich defects of atomic vacancies, nanoscale pinholes and distorted edges were formed within ultrathin MoS_2 nanosheets. Impressively, this integrated electrode with an ultralow MoS_2 loading of 0.14 mg/cm^2 can achieve small cell voltages of 1.96 and 2.25 V under 1 and 2 A/cm^2, respectively, in a practical PEMEC, superior to almost all cell performances of non-precious HER catalysts even with extremely high

loadings of 3–6 mg/cm^2 under the similar cell operation conditions. This work builds up a bridge to connect catalyst optimization to electrode fabrication, and offers a new opportunity to concurrently enhance the intrinsic catalytic activity, whole electrode conductivity and electrochemical stability for hydrogen production under high current densities in practical water electrolyzers.

CRediT authorship contribution statement

Zhiqiang Xie: Conceptualization, Methodology, Data curation, Writing – original draft, Writing – review & editing, Investigation, Validation. **Shule Yu**: Methodology, Investigation, Validation, Writing – review & editing. **Xiaohan Ma**: Methodology, Investigation, Validation, Writing – review & editing. **Kui Li**: Investigation, Writing – review & editing. **Lei Ding**: Methodology, Writing – review & editing. **Weitian Wang**: Investigation, Validation, Writing – review & editing. **David A. Cullen**: Resources, Methodology, Data curation, Investigation, Validation, Writing – review & editing. **Harry M. Meyer III**: Writing – review & editing. **Haoran Yu**: Methodology, Data curation, Investigation, Validation, Writing – review & editing. **Jianhua Tong**: Writing – review & editing. **Zili Wu**: Validation, Writing – review & editing. **Feng-Yuan Zhang**: Resources, Supervision, Project administration, Funding acquisition, Writing – review & editing.

Declaration of Competing Interest

The authors declare that they have no known competing financial interests or personal relationships that could have appeared to influence the work reported in this paper.

Acknowledgements

The authors greatly appreciate the support from U.S. Department of Energy's Office of Energy Efficiency and Renewable Energy (EERE) under the Fuel Cell Technologies Office Award Number DE-EE0008426 and DE-EE0008423 and National Energy Technology Laboratory under Award DE-FE0011585. A portion of the research including the synthesis, Raman and STEM was supported by the Center for Nanophase Materials Sciences (CNMS), which is a US Department of Energy, Office of Science User Facility at Oak Ridge National Laboratory. The authors also would like to appreciate Dr. Zhenghong Bao, Dr. Scott T. Retterer, Dale Hensley, Dayrl Briggs, Alexander Terekhov, Douglas Warnberg, and Dr. Brian Canfield for their help.

Appendix A. Supporting information

Supplementary data associated with this article can be found in the online version at doi:10.1016/j.apcatb.2022.121458.

References

[1] A. Lim, J. Kim, H.J. Lee, H.-J. Kim, S.J. Yoo, J.H. Jang, H. Young Park, Y.-E. Sung, H.S. Park, Low-loading IrO2 supported on Pt for catalysis of PEM water electrolysis and regenerative fuel cells, Appl. Catal. B Environ. 272 (2020), 118955.
[2] D. Song, J. Zheng, N.V. Myung, J. Xu, M. Zhang, Sandwich-type electrochemical immunosensor for CEA detection using magnetic hollow Ni/C@SiO2 nanomatrix and boronic acid functionalized CPS@PANI@Au probe, Talanta 225 (2021), 122006.
[3] Z. Chen, X. Duan, W. Wei, S. Wang, B.-J. Ni, Electrocatalysts for acidic oxygen evolution reaction: achievements and perspectives, Nano Energy 78 (2020), 105392.
[4] C.V. Pham, M. Bühler, J. Knöppel, M. Bierling, D. Seeberger, D. Escalera-López, K. J.J. Mayrhofer, S. Cherevko, S. Thiele, IrO2 coated TiO2 core-shell microparticles advance performance of low loading proton exchange membrane water electrolyzers, Appl. Catal. B Environ. 269 (2020), 118762.
[5] Z. Xie, S. Yu, G. Yang, K. Li, L. Ding, W. Wang, D.A. Cullen, H.M. Meyer, S. T. Retterer, Z. Wu, J. Sun, P.-X. Gao, F.-Y. Zhang, Ultrathin platinum nanowire based electrodes for high-efficiency hydrogen generation in practical electrolyzer cells, Chem. Eng. J. 410 (2021), 128333.
[6] C.V. Pham, D. Escalera-López, K. Mayrhofer, S. Cherevko, S. Thiele, Essentials of high performance water electrolyzers – from catalyst layer materials to electrode engineering, Adv. Energy Mater. 11 (44) (2021), 2101998.
[7] T. Lim, S.-K. Kim, Non-precious hydrogen evolution reaction catalysts: stepping forward to practical polymer electrolyte membrane-based zero-gap water electrolyzers, Chem. Eng. J. (2021), 133681.
[8] H. Huang, H. Kim, A. Lee, S. Kim, W.-G. Lim, C.-Y. Park, S. Kim, S.-K. Kim, J. Lee, Structure engineering defective and mass transfer-enhanced RuO2 nanosheets for proton exchange membrane water electrolyzer, Nano Energy 88 (2021), 106276.
[9] S. Wang, H. Lv, F. Tang, Y. Sun, W. Ji, W. Zhou, X. Shen, C. Zhang, Defect engineering assisted support effect:IrO2/N defective g-C3N4 composite as highly efficient anode catalyst in PEM water electrolysis, Chem. Eng. J. 419 (2021), 129455.
[10] G. Yang, S. Yu, Z. Kang, Y. Li, G. Bender, B.S. Pivovar, J.B. Green Jr., D.A. Cullen, F.-Y. Zhang, Building electron/proton nanohighways for full utilization of water splitting catalysts, Adv. Energy Mater. 10 (16) (2020), 1903871.
[11] T.T. Yang, T.L. Tan, W.A. Saidi, High activity toward the hydrogen evolution reaction on the edges of MoS2-supported platinum nanoclusters using cluster expansion and electrochemical modeling, Chem. Mater. 32 (3) (2020) 1315–1321.
[12] L. Sun, M. Gao, Z. Jing, Z. Cheng, D. Zheng, H. Xu, Q. Zhou, J. Lin, 1 T-Phase enriched P doped WS2 nanosphere for highly efficient electrochemical hydrogen evolution reaction, Chem. Eng. J. 429 (2022), 132187.
[13] G.L. Cardoso, P.C. Piquini, R. Ahuja, From monolayers to nanotubes: toward catalytic transition-metal dichalcogenides for hydrogen evolution reaction, Energy Fuels 35 (7) (2021) 6282–6288.
[14] N. Abidi, A. Bonduelle-Skrzypczak, S.N. Steinmann, How stable are 2H-MoS2 edges under hydrogen evolution reaction conditions? J. Phys. Chem. C 125 (31) (2021) 17058–17067.
[15] Hy Jung, Mj Chae, Jh Park, Yi Song, Jc Ro, Sj Suh, Effects of platinum group metals on MoS2 nanosheets for a high-performance hydrogen evolution reaction catalyst, ACS Appl. Energy Mater. 4 (10) (2021) 10748–10755.
[16] T. Rao, H. Wang, Y.-J. Zeng, Z. Guo, H. Zhang, W. Liao, Phase transitions and water splitting applications of 2D transition metal dichalcogenides and metal phosphorous trichalcogenides, Adv. Sci. 8 (10) (2021), 2002284.
[17] J. Luxa, L. Spejchalová, I. Jakubec, Z. Sofer, MoS2 stacking matters: 3R polytype significantly outperforms 2H MoS2 for the hydrogen evolution reaction, Nanoscale 13 (46) (2021) 19391–19398.
[18] S. Geng, W. Yang, Y. Liu, Y. Yu, Engineering sulfur vacancies in basal plane of MoS2 for enhanced hydrogen evolution reaction, J. Catal. 391 (2020) 91–97.
[19] G. Li, Z. Chen, Y. Li, D. Zhang, W. Yang, Y. Liu, L. Cao, Engineering substrate interaction to improve hydrogen evolution catalysis of monolayer MoS2 films beyond Pt, ACS Nano 14 (2) (2020) 1707–1714.
[20] J. Hu, C. Zhang, P. Yang, J. Xiao, T. Deng, Z. Liu, B. Huang, M.K.H. Leung, S. Yang, Kinetic-oriented construction of MoS2 synergistic interface to boost pH-universal hydrogen evolution, Adv. Funct. Mater. 30 (6) (2020), 1908520.
[21] H. Wang, X. Xiao, S. Liu, C.-L. Chiang, X. Kuai, C.-K. Peng, Y.-C. Lin, X. Meng, J. Zhao, J. Choi, Y.-G. Lin, J.-M. Lee, L. Gao, Structural and electronic optimization of MoS2 edges for hydrogen evolution, J. Am. Chem. Soc. 141 (46) (2019) 18578–18584.
[22] X. Wang, Y. Zhang, H. Si, Q. Zhang, J. Wu, L. Gao, X. Wei, Y. Sun, Q. Liao, Z. Zhang, K. Ammarah, L. Gu, Z. Kang, Y. Zhang, Single-atom vacancy defect to trigger high-efficiency hydrogen evolution of MoS2, J. Am. Chem. Soc. 142 (9) (2020) 4298–4308.
[23] W. Wu, C. Niu, C. Wei, Y. Jia, C. Li, Q. Xu, Activation of MoS2 basal planes for hydrogen evolution by zinc, Angew. Chem. 131 (7) (2019) 2051–2055.
[24] Q. Xu, Y. Liu, H. Jiang, Y. Hu, H. Liu, C. Li, Unsaturated sulfur edge engineering of strongly coupled MoS2 nanosheet–carbon macroporous hybrid catalyst for enhanced hydrogen generation, Adv. Energy Mater. 9 (2) (2019), 1802553.
[25] Y. Cao, Roadmap and direction toward high-performance MoS2 hydrogen evolution catalysts, ACS Nano 15 (7) (2021) 11014–11039.
[26] Y. He, P. Tang, Z. Hu, Q. He, C. Zhu, L. Wang, Q. Zeng, P. Golani, G. Gao, W. Fu, Z. Huang, C. Gao, J. Xia, X. Wang, X. Wang, C. Zhu, Q.M. Ramasse, A. Zhang, B. An, Y. Zhang, S. Martí-Sánchez, J.R. Morante, L. Wang, B.K. Tay, B.I. Yakobson, A. Trampert, H. Zhang, M. Wu, Q.J. Wang, J. Arbiol, Z. Liu, Engineering grain boundaries at the 2D limit for the hydrogen evolution reaction, Nat. Commun. 11 (1) (2020) 57.
[27] X. Zhang, H. Li, H. Yang, F. Xie, Z. Yuan, L. Zajickova, W. Li, Phase-engineering of 1T/2H molybdenum disulfide by using ionic liquid for enhanced electrocatalytic hydrogen evolution, ChemElectroChem 7 (15) (2020) 3347–3352.
[28] Y. Chen, J. Rong, Q. Tao, C. Xing, M. Lian, J. Cheng, X. Liu, J. Cao, M. Wei, S. Lv, P. Zhu, L. Yang, J. Yang, Modifying microscopic structures of MoS2 by high pressure and high temperature used in hydrogen evolution reaction, Electrochim. Acta 357 (2020), 136868.
[29] Y. Zhang, Y. Kuwahara, K. Mori, C. Louis, H. Yamashita, Hybrid phase 1T/2H-MoS2 with controllable 1T concentration and its promoted hydrogen evolution reaction, Nanoscale 12 (22) (2020) 11908–11915.
[30] S. Wang, J. Li, S. Hu, H. Kang, S. Zhao, R. Xiao, Y. Sui, Z. Chen, S. Peng, Z. Jin, X. Liu, Y. Zhang, G. Yu, Morphology regulation of MoS2 nanosheet-based domain boundaries for the hydrogen evolution reaction, ACS Appl. Nano Mater. (2022).
[31] J. Wei, P. He, J. Wu, N. Chen, T. Xu, E. Shi, C. Pan, X. Zhao, Y. Zhang, Conversion of 2H MoS2 to 1 T MoS2 via lithium ion doping: Effective removal of elemental mercury, Chem. Eng. J. 428 (2022), 131014.
[32] B. Gao, Y. Zhao, X. Du, D. Li, S. Ding, Y. Li, C. Xiao, Z. Song, Electron injection induced phase transition of 2H to 1T MoS2 by cobalt and nickel substitutional doping, Chem. Eng. J. 411 (2021), 128567.

[33] J. Xu, Z. Zhao, W. Wei, G. Chang, Z. Xie, W. Guo, D. Liu, D. Qu, H. Tang, J. Li, Tuning the intrinsic activity and electrochemical surface area of MoS2 via tiny Zn doping: toward an efficient hydrogen evolution reaction (HER) catalyst, Chem. Eur. J. 27 (64) (2021) 15992–15999.
[34] K. Le, X. Zhang, Q. Zhao, Y. Liu, P. Yi, S. Xu, W. Liu, Controllably doping nitrogen into 1T/2H MoS2 heterostructure nanosheets for enhanced supercapacitive and electrocatalytic performance by low-power N2 plasma, ACS Appl. Mater. Interfaces 13 (37) (2021) 44427–44439.
[35] W. Chen, Z. Wang, K.V. Bets, D.X. Luong, M. Ren, M.G. Stanford, E.A. McHugh, W. A. Algozeeb, H. Guo, G. Gao, B. Deng, J. Chen, J.T. Li, W.T. Carsten, B.I. Yakobson, J.M. Tour, Millisecond conversion of metastable 2D materials by flash joule heating, ACS Nano 15 (1) (2021) 1282–1290.
[36] P.K.R. Holzapfel, M. Bühler, D. Escalera-López, M. Bierling, F.D. Speck, K.J. J. Mayrhofer, S. Cherevko, C.V. Pham, S. Thiele, Fabrication of a robust PEM water electrolyzer based on non-noble metal cathode catalyst: [Mo3S13]2− clusters anchored to N-doped carbon nanotubes, Small 16 (37) (2020), 2003161.
[37] J. Ampurdanés, M. Chourashiya, A. Urakawa, Cobalt oxide-based materials as non-PGM catalyst for HER in PEM electrolysis and in situ XAS characterization of its functional state, Catal. Today 336 (2019) 161–168.
[38] J. Mo, S. Wu, T.H.M. Lau, R. Kato, K. Suenaga, T.S. Wu, Y.L. Soo, J.S. Foord, S.C. E. Tsang, Transition metal atom–doped monolayer MoS2 in a proton-exchange membrane electrolyzer, Mater. Today Adv. 6 (2020), 100020.
[39] T. Corrales-Sánchez, J. Ampurdanés, A. Urakawa, MoS2-based materials as alternative cathode catalyst for PEM electrolysis, Int. J. Hydrog. Energy 39 (35) (2014) 20837–20843.
[40] C.D. Giovanni, Á. Reyes-Carmona, A. Coursier, S. Nowak, J.M. Grenèche, H. Lecoq, L. Mouton, J. Rozière, D. Jones, J. Peron, M. Giraud, C. Tard, Low-cost nanostructured iron sulfide electrocatalysts for PEM water electrolysis, ACS Catal. 6 (4) (2016) 2626–2631.
[41] Z. Liu, Z. Gao, Y. Liu, M. Xia, R. Wang, N. Li, Heterogeneous nanostructure based on 1T-Phase MoS2 for enhanced electrocatalytic hydrogen evolution, ACS Appl. Mater. Interfaces 9 (30) (2017) 25291–25297.
[42] Z. Lei, J. Zhan, L. Tang, Y. Zhang, Y. Wang, Recent development of metallic (1T) phase of molybdenum disulfide for energy conversion and storage, Adv. Energy Mater. 8 (19) (2018), 1703482.
[43] R. Peng, L. Liang, Z.D. Hood, A. Boulesbaa, A. Puretzky, A.V. Ievlev, J. Come, O. S. Ovchinnikova, H. Wang, C. Ma, M. Chi, B.G. Sumpter, Z. Wu, In-plane heterojunctions enable multiphasic two-dimensional (2D) MoS2 nanosheets as efficient photocatalysts for hydrogen evolution from water reduction, ACS Catal. 6 (10) (2016) 6723–6729.
[44] C. Tsai, H. Li, S. Park, J. Park, H.S. Han, J.K. Nørskov, X. Zheng, F. Abild-Pedersen, Electrochemical generation of sulfur vacancies in the basal plane of MoS2 for hydrogen evolution, Nat. Commun. 8 (2017) 15113.
[45] G. Ye, Y. Gong, J. Lin, B. Li, Y. He, S.T. Pantelides, W. Zhou, R. Vajtai, P.M. Ajayan, Defects engineered monolayer MoS2 for improved hydrogen evolution reaction, Nano Lett. 16 (2) (2016) 1097–1103.
[46] Y. Liu, Y. Li, F. Peng, Y. Lin, S. Yang, S. Zhang, H. Wang, Y. Cao, H. Yu, 2H- and 1T-mixed phase few-layer MoS2 as a superior to Pt co-catalyst coated on TiO2 nanorod arrays for photocatalytic hydrogen evolution, Appl. Catal. B Environ. 241 (2019) 236–245.
[47] K. Wu, X. Cao, M. Li, B. Lei, J. Zhan, M. Wu, Bottom-up synthesis of MoS2/CNTs hollow polyhedron with 1T/2H hybrid phase for superior potassium-ion storage, Small 16 (43) (2020), 2004178.
[48] J.-C.E. Yang, M.-P. Zhu, X. Duan, S. Wang, B. Yuan, M.-L. Fu, The mechanistic difference of ^{1}T–^{2}H MoS2 homojunctions in persulfates activation: structure-dependent oxidation pathways, Appl. Catal. B Environ. 297 (2021), 120460.
[49] X. Liu, R. Guo, K. Ni, F. Xia, C. Niu, B. Wen, J. Meng, P. Wu, J. Wu, X. Wu, L. Mai, Reconstruction-determined alkaline water electrolysis at industrial temperatures, Adv. Mater. 32 (40) (2020), 2001136.
[50] X. Liu, J. Meng, J. Zhu, M. Huang, B. Wen, R. Guo, L. Mai, Comprehensive understandings into complete reconstruction of precatalysts: synthesis, applications, and characterizations, Adv. Mater. 33 (32) (2021), 2007344.
[51] L.A. Adofo, H.J. Kim, F.O.-T. Agyapong-Fordjour, H.T. Thanh Nguyen, J.W. Jin, Y. I. Kim, S.J. Kim, J.H. Kim, S. Boandoh, S.H. Choi, S.J. Lee, S.J. Yun, Y.-M. Kim, S. M. Kim, Y.-K. Han, K.K. Kim, Hydrogen evolution reaction catalyst with high catalytic activity by interplay between organic molecules and transition metal dichalcogenide monolayers, Mater. Today Energy 25 (2022), 100976.